SIAM J. SCI. COMPUT.
Vol. 43, No. 3, pp. B598–B622

A HIGH ORDER FINITE DIFFERENCE WEIGHTED ESSENTIALLY NONOSCILLATORY SCHEME WITH A KERNEL-BASED CONSTRAINED TRANSPORT METHOD FOR IDEAL MAGNETOHYDRODYNAMICS*

FIRAT CAKIR†, ANDREW CHRISTLIEB‡, AND YAN JIANG§

Abstract. The ideal magnetohydrodynamics equations are challenging because one needs to maintain the divergence-free condition, $\nabla \cdot \mathbf{B} = 0$. Many numerical methods have been developed to enforce this condition. In this paper, we extend our work on mesh aligned constrained transport by developing a new approach for the vector potential in two and three dimensions. The approach for solving the vector potential is based on the method of lines transpose and is A-stable, eliminating the need for diffusion limiters needed in our previous work in three dimensions. For problems with strong shocks, this approach offers considerable improvements when compared with our previous version of constrained transport. The method is robust and has been tested on the 2D and 3D cloud shock, blast wave, and field loop problems.

Key words. magnetohydrodynamics, constrained transport method, kernel-based scheme, plasma physics

AMS subject classifications. 35L40, 65M99, 76L05, 76W05, 70H20

DOI. 10.1137/19M1278958

1. Introduction.

The ideal magnetohydrodynamics (MHD) equations are one of the most important classical models of plasma physics explaining the macroscopic phenomena of a quasi-neutral plasma system. The model contains a set of transport evolution equations for the quantities of mass, momentum, and energy density as well as the magnetic field in a conducting fluid. Mathematically, the MHD equations are a system of nonlinear hyperbolic conservation laws. What makes the MHD equations challenging is the need to ensure that the magnetic field satisfies the divergence-free condition over the duration of the simulation. While the MHD equations are hyperbolic, standard numerical methods for hyperbolic conservation laws fail to guarantee $\nabla \cdot \mathbf{B} = 0$. Among the many approaches proposed to satisfy the involution $\nabla \cdot \mathbf{B} = 0$, there are four dominant approaches in the literature: 8-wave formulation [40, 41], projection methods [4, 46], hyperbolic divergence cleaning methods [23], and constrained transport methods [47, 26, 21, 43, 7, 46, 37, 22, 27, 38, 2, 45, 42, 30, 20, 19, 44].

This work introduces a new high order method to satisfy the involution based on an unstaggered constrained transport (CT) methodology. The original CT method is considered to be a modification of the Yee method [48], from electromagnetics, adapted for the ideal MHD equations. In the original CT methodology, staggered electric and magnetic fields are used to create appropriate finite difference operators.

*Submitted to the journal's Computational Methods in Science and Engineering section August 5, 2019; accepted for publication (in revised form) January 7, 2021; published electronically May 18, 2021.

https://doi.org/10.1137/19M1278958

Funding: The work of the second author was supported by NSF grant DMS-1912183. The work of the third author was supported by NSFC grant 11901555.

†Department of Mathematics, Michigan State University, East Lansing, MI 48824 USA (cakirfir@msu.edu).

‡Department of Computational Mathematics, Science and Engineering, Department of Mathematics and Department of Electrical Engineering, Michigan State University, East Lansing, MI 48824 USA (christli@msu.edu).

§School of Mathematical Sciences, University of Science and Technology of China, Hefei, Anhui, 230026, People's Republic of China (jiangy@ustc.edu.cn).

These operators eventually lead to a globally divergence-free magnetic field. But as with the Yee method, including geometry in a problem is challenging for this approach.

In the literature, various modifications of the CT methodology have been presented. In particular, high resolution shock capturing schemes have been a primary focus. DeVore [24] presented an application of a flux corrected transport approach that satisfies a divergence-free magnetic field. There are a range of approaches for building the electric field using Ohm's law in a CT methodology, including those presented by Balsara and Spicer [7], Dai and Woodard [21], and Ryu et al. [43]. Londrillo and Del Zanna [37, 38] constructed one of the first high order upwind schemes building on the work of Evans and Hawley. De Sterck [22] introduced a similar CT scheme on unstructured triangle grids based on multidimensional upwind advection schemes. Balsara [1] described a divergence-free adaptive mesh refinement (AMR) method utilizing a CT approach. Tóth [46] compared several schemes that maintained the divergence-free condition. This work demonstrated that the use of a staggered magnetic field is unnecessary and, instead, focused on developing unstaggered methods for CT.

Unstaggered CT schemes have garnered increasing attention over the last few years. Mesh aligned CT is not a new idea. Wilson [47] and Dorfi [25] were some of the first to investigate the use of magnetic vector potential equations for a CT solution to the MHD equations. However, modern shock capturing strategies were not used in those works resulting in strong numerical diffusion. Londrillo and Del Zanna [37] used the magnetic potential solutions in the context of shock capturing methods, along with De Sterck [22] and Londrillo and Del Zanna [38]. Fey and Torrilhon [27] developed one of the only unstaggered upwind methods satisfying the divergence-free constraint in two dimensions for a direct update of the magnetic field. Rossmanith [42] designed an ustaggered wave propagation scheme for MHD flows, based on the algorithms in [35], using a CT method to maintain a divergence-free magnetic field. Helzel, Rossmarith, and Taetz [30, 31] generalized the 2D unstaggered CT work to 3D MHD equations so that the method is applicable on both Cartesian and rectangular mapped grids.

The efficiency gains attributed to the use of high order methods, in a multicore computing setting, has motivated the development of high order schemes for the ideal MHD equations. Balsara [3] designed third order, divergence-free, weighted essentially nonoscillatory (WENO) methods for MHD equations using a Runge–Kutta method with a staggered magnetic field. Balsara et al. [5, 6] introduced high accurate ADER (Arbitrary DERivative)-WENO schemes for divergence-free MHD on structured meshes, again using a staggered magnetic field. Li et al. [36, 28] and Cheng et al. [14] developed central discontinuous Galerkin schemes for the ideal MHD equations, which satisfy the divergence-free constraint globally. These methods utilize primal and dual overlapping meshes and employ a different discretization for the magnetic induction equations. Kawai [34] introduced a divergence-free high order accurate finite difference scheme which has an effective shock capturing capability for the MHD equations. The method is capable of capturing discontinuous behavior in the magnetic field through the construction of artificial diffusion terms.

In our previous papers [20, 19, 44], we introduced a high order finite difference WENO for the ideal MHD, in two and three dimensions, by developing unstaggered CT methodology for the vector potential $\mathbf{A}$, which is fifth order in space and third order in time. We choose to solve the magnetic vector potential under the Weyl gauge, which makes the vector potential a weakly hyperbolic system. The vector potential in two dimensions is a Hamilton–Jacobi (HJ) equation and in three dimensions resembles a modified HJ equation. In [20], WENO is applied to the central derivative of $\mathbf{A}$,

instead of the flux values at the grid points, to approximate the one-sided partial derivative terms A_x^- and A_x^+ that appear in the HJ equation. In three dimensions, if explicit time stepping is used with the vector potential, the additional terms in the modified HJ equation resemble a convection reaction equation. This system tends to be unstable. To remedy this issue, in [20], we introduced an artificial resistivity terms for the 3D case to stabilize it and to control unphysical oscillations in the magnetic field.

In this paper, we build on our work [20, 19, 44] on mesh aligned CT by developing a new approach for the magnetic vector potential to solve the ideal MHD equations in two and three dimensions. The approach uses a kernel-based numerical scheme [16, 17], which is derived from the method of lines transpose (MOL^T) [10, 13, 12, 15, 11]. A novel discretization for the spatial operator is applied that uses a convolution integral with a specific kernel. This formulation converts local operators, i.e., derivatives, into global representations using convolutions with kernels, i.e. Green's functions, and is similar, in spirit, to taking a fast Fourier transform. This approximation to the spatial operator provably yields a high order discretization of the HJ equation, which is unconditionally stable for linear problems, and it behaves unconditionally stable for nonlinear problems, such as the magnetic vector potential. Using ideas from fast summation, the complexity of the method can be shown to be $O(N)$ and is as fast as an explicit method, such as the Yee scheme for electromagnetics [13, 11]. Within this methodology, we update the predicted magnetic field obtained from the base scheme using a corrected divergence-free magnetic field. The approach for solving the vector potential is derived from our work in [17], eliminates the necessity of diffusion limiters introduced in our previous work in three dimensions, [20], since the method employed here appears to be unconditionally stable. The corrected magnetic field is computed by fourth order accurate central finite difference operators that approximate the curl of the magnetic vector potential. Our solver for the vector potential is coupled with the fifth order finite difference WENO scheme of Jiang and Shu [33] as the base scheme for the ideal MHD equations. Third order explicit strong stability preserving (SSP) Runge–Kutta (RK) time stepping is used for the time discretization. The work presented here offers a number of improvements over the previous method, especially in the context of strong shocks. The primary benefit is that the proposed approach eliminates the diffusion limiters required by our previous work. This method is robust and has been tested on the 2D and 3D cloud shock, blast wave, and field loop problems.

The rest of this paper is organized as follows: in section 2, we briefly review the MHD equations, CT method, and the evolution of the magnetic vector equations; in section 3, we present our novel numerical scheme for 1D HJ equations and the multi-dimensional solver; the resulting 2D and 3D schemes are tested on several numerical problems in section 4; in section 5, we summarize the conclusions of the work.

2. The ideal MHD equations. In this section we present a brief review of the ideal MHD equations, which is a first order hyperbolic system of conservation laws, as well as the base CT methodology we employ in solving this system of equations. The conservative form of the ideal MHD equations can be written as

$$\partial_t \begin{bmatrix} \rho \\ \rho\mathbf{u} \\ \mathcal{E} \\ \mathbf{B} \end{bmatrix} + \nabla \cdot \begin{bmatrix} \rho\mathbf{u} \\ \rho\mathbf{u} \otimes \mathbf{u} + p_{\text{tot}}\mathbb{I} - \mathbf{B} \otimes \mathbf{B} \\ \mathbf{u}(\mathcal{E} + p_{\text{tot}}) - \mathbf{B}(\mathbf{u} \cdot \mathbf{B}) \\ \mathbf{u} \otimes \mathbf{B} - \mathbf{B} \otimes \mathbf{u} \end{bmatrix} = 0, \tag{2.1}$$

$$\nabla \cdot \mathbf{B} = 0 \tag{2.2}$$

with the equation of state as

$$\mathcal{E} = \frac{p}{\gamma - 1} + \frac{\rho \|\mathbf{u}\|^2}{2} + \frac{\|\mathbf{B}\|^2}{2}, \tag{2.3}$$

where the total mass ρ, the momentum $\rho\mathbf{u} = (\rho u^1, \rho u^2, \rho u^3)^T$, the energy densities $\mathcal{E}$ of the plasma system, and the magnetic field vector $\mathbf{B} = (B^1, B^2, B^3)^T$ are all conserved variables. The velocity $\mathbf{u}$ and the total pressure $p_{\text{tot}} = p + \frac{1}{2}\|\mathbf{B}\|^2$, together with the hydrodynamic pressure, which is given by the ideal gas law as

$$p = (\gamma - 1)\left(\mathcal{E} - \frac{1}{2}\|\mathbf{B}\|^2 - \frac{1}{2}\rho\|\mathbf{u}\|^2\right), \tag{2.4}$$

are derived quantities. $\gamma = 5/3$ is the ideal gas constant, and the notation $\|\cdot\|$ is used for the purpose of the Euclidean vector norm. The MHD equations (2.1)–(2.2) are derived and discussed in many standard plasma textbooks (e.g., [39]).

2.1. Outline of the CT methodology. The major challenge when dealing with the numerical solution of the system (2.1)–(2.3) is to satisfy the divergence-free condition (2.2). Although there is a variety of approaches to enforce this condition, this work uses the CT method. Here we outline our high order CT framework.

The idea of CT is to advance the conserved variables $\mathbf{q} = (\rho, \rho\mathbf{u}, \mathcal{E}, \mathbf{B})$ in a formulation that does not require a projection or the introduction of artifactual terms. In the mesh aligned formulation presented here, we will make use of the magnetic vector potential, $\mathbf{A}$, which we outline in the next section. For our outline of CT, we note that $\mathbf{B} = \nabla \times \mathbf{A}$ and that given $\mathbf{A}$, a fourth order central difference will produce a provably locally divergence-free solution to $\mathbf{B}$. Consider a semidiscrete system of ordinary differential equations for MHD equations (2.1)

$$\mathbf{q}'_{mhd}(t) = \mathcal{L}_1(\mathbf{q}_{mhd}(t)), \tag{2.5}$$

where $\mathbf{q}_{mhd}(t)$ represents the grid function at time t consisting of all pointwise values of the conserved quantities in the ideal MHD system $\mathbf{q}_{mhd} = (\rho, \rho\mathbf{u}, \mathcal{E}, \mathbf{B})$. In our work, the details about $\mathcal{L}_1(\mathbf{q}_{mhd}(t))$ are based on the finite difference WENO method, which are presented in [20]. And the high order SSP RK method is used for temporal discretization of the ideal MHD.

In the next section we will present the formulation of $\mathbf{A}$ and then the update. Given that we have this $\mathbf{A}$, a locally divergence-free version of $\mathbf{B}$ is given by a fourth order central difference curl of $\mathbf{A}$. The key steps advancing the solution from its current time step $t = t^n$ (or the initial condition at t^0) to its new time step t^{n+1} are listed below:

- Step 0: Start with the given current time step $\mathbf{q}^n_{mhd} = (\rho^n, \rho\mathbf{u}^n, \mathcal{E}^n, \mathbf{B}^n)^T$ and $\mathbf{A}^n$.
- Step 1: Obtain $\mathbf{q}^*_{mhd}$ and $\mathbf{A}^{n+1}$ separately, where

  $$\mathbf{q}^*_{mhd} = \left(\rho^{n+1}, \rho^{n+1}\mathbf{u}^{n+1}, \mathcal{E}^*, \mathbf{B}^*\right).$$

  Here, $\mathcal{E}^*$ and $\mathbf{B}^*$ are given with a $*$ superscript instead of $n+1$ to indicate that the predicted $\mathbf{B}$ and $\mathcal{E}$ will be corrected by a predictor-corrector constrained transpose method before the end of the time step.
- Step 2: Replace $\mathbf{B}^*$ to $\mathbf{B}^{n+1}$ by a discrete curl of $\mathbf{A}^{n+1}$, for instance, using a fourth order central difference,

  $$\mathbf{B}^{n+1} = \nabla \times \mathbf{A}^{n+1}.$$

- Step 3: Set the corrected total energy density value $\mathcal{E}^{n+1}$ based on one of the following options:

  Option 1: Keep the total energy conserved:

$$\mathcal{E}^{n+1} = \mathcal{E}^*.$$

  Option 2: Keep the pressure the same after updating the magnetic field:

$$\mathcal{E}^{n+1} = \mathcal{E}^* + \frac{1}{2}(\left\|\mathbf{B}^{n+1}\right\|^2 - \|\mathbf{B}^*\|^2).$$

  (Option 2 sometimes helps to prevent negative pressure).

We now describe the formulation of $\mathbf{A}$ and how we constraint the update for $\mathbf{A}^{n+1}$ using our kernel-based approach.

2.2. Magnetic vector potential. There have been many numerical methods presented in the literature for numerically solving the MHD system, but a high order version that addresses the main challenge of satisfying the divergence-free condition on the magnetic field while easily embedding into AMR has remained plusive. Here, we will derive the magnetic vector potential equation from the magnetic field equation given in the (2.1)–(2.2) system. This will serve as the foundation of our CT framework.

Since the magnetic field is divergence-free, it can always be written as the curl of a magnetic vector potential:

$$\mathbf{B} = \nabla \times \mathbf{A}. \tag{2.6}$$

The key step of the CT scheme is to solve the magnetic potential for correcting the magnetic field. The evolution of the magnetic field in (2.1) can be written in the following form:

$$\mathbf{B}_t + \nabla \times (\mathbf{B} \times \mathbf{u}) = 0, \tag{2.7}$$

using the relation

$$\nabla \cdot (\mathbf{u} \otimes \mathbf{B} - \mathbf{B} \otimes \mathbf{u}) = \nabla \times (\mathbf{B} \times \mathbf{u}).$$

Since $\mathbf{B}$ is divergence-free, we set $\mathbf{B} = \nabla \times \mathbf{A}$ and rewrite the evolution equation (2.7) as

$$\nabla \times \left\{\mathbf{A}_t + (\nabla \times \mathbf{A}) \times \mathbf{u}\right\} = 0.$$

This implies that there exists a scalar function ψ such that

$$\mathbf{A}_t + (\nabla \times \mathbf{A}) \times \mathbf{u} = -\nabla\psi.$$

There are various choices of the gauge conditions depending on how we chose the ψ. Helzel, Rossmanith, and Taetz [30] showed that using the Weyl gauge, i.e., setting $\psi \equiv 0$, one can achieve stable solutions. This condition results in the evolution equation for the magnetic vector potential, which can be written as

$$\partial_t \mathbf{A} + N_1 \mathbf{A}_x + N_2 \mathbf{A}_y + N_3 \mathbf{A}_z = 0 \tag{2.8}$$

with

$$N_1 = \begin{bmatrix} 0 & -u^2 & -u^3 \\ 0 & u^1 & 0 \\ 0 & 0 & u^1 \end{bmatrix}, \quad N_2 = \begin{bmatrix} u^2 & 0 & 0 \\ -u^1 & 0 & -u^3 \\ 0 & 0 & u^2 \end{bmatrix}, \quad N_3 = \begin{bmatrix} u^3 & 0 & 0 \\ 0 & u^3 & 0 \\ -u^1 & -u^2 & 0 \end{bmatrix}.$$

As discussed in [30, 20], the resulting system is only weakly hyperbolic since the matrix of right eigenvectors of the flux Jacobian doesn't have full rank in certain directions. Hence our approach for solving the vector potential equations will rely on an alternative discretization strategy that comes from studying HJ equations discussed in section 3.

2.3. The proposed advantage of the new kernel-based method over the previous finite difference WENO-HJ method. In this section, we outline the advantage of our new CT method over our previous work [20].

The vector potential formulation in three dimensions is close to being a standard HJ equation and in two dimensions is an HJ equation. For three dimensions, our previous method, [20], required a stabilization. Consider the first component of (2.8) in three dimensions:

$$A^1_t - u^2 A^2_x - u^3 A^3_x + u^2 A^1_y + u^3 A^1_z = \epsilon^1 \frac{\partial^2 A^1}{\partial x^2}\ , \tag{2.9}$$

where ϵ^1 adjusts the strength of the diffusion limiter used in [20]. ϵ^1 depends on a smoothness indicator and is zero in smooth parts of the domain; see reference [20] for details. The issue is that the vector potential is weakly hyperbolic and there can be issues of stability at strong shocks or unphysical oscillations. This is a natural consequence of the fact there is no obvious or direct way to add limiters into the weakly hyperbolic formulation [20, 30, 31]. The above equation obeys the structure of an HJ equation except for the two terms $\partial_x A^2$ and $\partial_x A^3$. In [20, 30, 31], stabilization and limiting of unphysical oscillations are achieved through the use of a local diffusion limiter, as above. This limiter is used in a small number of regions of the domain, where there are either discontinuities or strong shocks. As discussed in [20], in two dimensions, where these terms do not exist, one does not need a diffusion limiter, and the base method works fine with a WENO-HJ discretization and no additional limiter.

In the current work, we will circumvent the stabilization challenges by introducing a new $O(N)$ implicit method for the magnetic potential equation without artificial resistivity terms. The rest of the scheme is still using the same WENO architecture used in the previous work. In the next section we present an overview of the MOL$^{\mathrm{T}}$, for HJ equations, which was presented in the previous work [17]. This formulation is the basis of our new approach to CT.

3. HJ equations. In this section we introduce the main ideas in our kernel-based method [16, 17], which is derived from the MOL^T [9, 10, 13, 12, 15, 11]. The simplest way to describe the MOL^T is as follows: we start by discretizing the problem in time; we then use a global approximation for the inherently local term (the derivative). By doing this, we are able to make an explicit approximation unconditionally stable. As for the global approximation, it is similar to an FFT, but with a different convolution kernel. The form of the approximation is what facilitates the stability of the method. Through the use of a three-term recurrence relation, the convolution integrals can be evaluated using $O(N)$ operations.

3.1. 1D HJ equations. We start with a 1D HJ equation,

$$A_t + H(A_x) = 0, \qquad A(x,0) = A^0(x), \qquad x \in [a,b], \tag{3.1}$$

where H is the Hamiltonian flux. For the time discretization, to evolve the solution from time t^n to t^{n+1}, we use the classical explicit SSP RK schemes [29]. In this work, we propose to use the following SSP RK schemes such as the first order forward Euler scheme,

$$A^{n+1} = A^n - \Delta t \hat{H}(A_x^{n,-}, A_x^{n,+}); \tag{3.2}$$

the second order SSP RK scheme,

$$\begin{aligned} A^{(1)} &= A^n - \Delta t \hat{H}(A_x^{n,-}, A_x^{n,+}), \\ A^{n+1} &= \frac{1}{2}A^n + \frac{1}{2}\left(A^{(1)} - \Delta t \hat{H}(A_x^{(1),-}, A_x^{(1),+})\right); \end{aligned} \tag{3.3}$$

and the third order SSP RK scheme,

$$\begin{aligned} A^{(1)} &= u^n - \Delta t \hat{H}(A_x^{n,-}, A_x^{n,+}), \\ A^{(2)} &= \frac{3}{4}A^n + \frac{1}{4}\left(A^{(1)} - \Delta t \hat{H}(A_x^{(1),-}, A_x^{(1),+})\right), \\ A^{n+1} &= \frac{1}{3}A^n + \frac{2}{3}\left(A^{(2)} - \Delta t \hat{H}(A_x^{(2),-}, A_x^{(2),+})\right). \end{aligned} \tag{3.4}$$

Here, Δt denotes the time step and $\hat{H}$ is the numerical Hamiltonian, i.e., the local Lax–Friedrichs Hamiltonian flux [32]:

$$\hat{H}(\phi^-, \phi^+) = H\left(\frac{\phi^- + \phi^+}{2}\right) - c(\phi^-, \phi^+)\frac{(\phi^+ - \phi^-)}{2} \tag{3.5}$$

with $c(\phi^-, \phi^+) = \max_{\phi \in [\min(\phi^-,\phi^+), \max(\phi^-,\phi^+)]} |H'(\phi)|$. A_x^- and A_x^+ are one-sided derivatives with *left*-biased and *right*-biased methods, respectively, to approximate A_x. Finding these derivatives is the dominant role in our work, and we will present the details of the construction of them in the following subsection.

3.2. Approximation of the first order derivative ∂_x. Approximating the partial spatial derivative terms with a kernel-based scheme is the major part of this work. In this section we briefly review the construction of the ∂_x derivative approximation using the kernel-based formulation established in [16]. We start by defining the basic tools needed for the construction of ∂_x. These tools will depend on operators $\mathcal{L}_L$ and $\mathcal{L}_R$ and their inverses $\mathcal{L}_L^{-1}$ and $\mathcal{L}_R^{-1}$ (defined below). In defining the inverse operators, we will need to incorporate boundary information. These operators will allow us to define ∂_x in terms of a convergent Neumann series containing the inverse operators $\mathcal{L}_L^{-1}$ and $\mathcal{L}_R^{-1}$. In other words, this redefines ∂_x as a sum of successively applied integrals, which we denote as the successive convolution approximation. With each additional integral that is added to the successive convolution approximation, the accuracy of our representations of ∂_x will be increased. Using fast summation, this will give an $O(N)$ approximation that is provably unconditionally stable for linear HJ equations when coupled with explicit RK time stepping.

Let's define operators $\mathcal{L}_L$ and $\mathcal{L}_R$ on the closed interval $[a, b]$ and their inverse operators

$$\mathcal{L}_L = \mathcal{I} + \frac{1}{\alpha}\partial_x \;\Rightarrow\; \mathcal{L}_L^{-1}[v, \alpha](x) = \alpha \int_a^x e^{-\alpha(x-y)} v(y) dy + A_L e^{-\alpha(x-a)}, \tag{3.6a}$$

$$\mathcal{L}_R = \mathcal{I} - \frac{1}{\alpha}\partial_x \;\Rightarrow\; \mathcal{L}_R^{-1}[v, \alpha](x) = \alpha \int_x^b e^{-\alpha(y-x)} v(y) dy + B_R e^{-\alpha(b-x)}, \tag{3.6b}$$

where $\mathcal{I}$ is the identity operator and α is a positive constant. We use I^L and I^R to denote the convolution integral as

$$I^L[v,\alpha](x) = \alpha \int_a^x e^{-\alpha(x-y)} v(y)dy, \quad I^R[v,\alpha](x) = \alpha \int_x^b e^{-\alpha(y-x)} v(y)dy. \tag{3.7}$$

We can see that I^L depends on the function values of v from the left end point a to x, and likewise with I^R. Also note that A_L and B_R are determined by the boundary conditions. For instance, if we assume periodic boundary conditions, i.e.,

$$\mathcal{L}_L^{-1}[v,\alpha](a) = \mathcal{L}_L^{-1}[v,\alpha](b) \quad \text{and} \quad \mathcal{L}_R^{-1}[v,\alpha](a) = \mathcal{L}_R^{-1}[v,\alpha](b),$$

then we obtain

$$A_L = \frac{I^L[v,\alpha](b)}{1-\mu} \quad \text{and} \quad B_R = \frac{I^R[v,\alpha](a)}{1-\mu}, \tag{3.8}$$

where $\mu = e^{-\alpha(b-a)}$. On the other hand, if we require

$$\mathcal{L}_L^{-1}[v,\alpha](a) = C_a \quad \text{and} \quad \mathcal{L}_R^{-1}[v,\alpha](b) = C_b$$

with given numbers C_a and C_b then the boundary coefficients are obtained as

$$A_L = C_a \quad \text{and} \quad B_R = C_b. \tag{3.9}$$

To define the Neumann series approximation to ∂_x, we now introduce two new operators $\mathcal{D}_L$ and $\mathcal{D}_R$:

$$\mathcal{D}_L = \mathcal{I} - \mathcal{L}_L^{-1} \quad \text{and} \quad \mathcal{D}_R = \mathcal{I} - \mathcal{L}_R^{-1}.$$

Then $\frac{1}{\alpha}\partial_x$ can be represented using the infinite series of these operators as

$$\frac{1}{\alpha}\partial_x = \mathcal{L}_L - \mathcal{I} = \mathcal{L}_L(\mathcal{I} - \mathcal{L}_L^{-1}) = \mathcal{D}_L(\mathcal{I} - \mathcal{D}_L)^{-1} = \sum_{p=1}^{\infty} \mathcal{D}_L^p, \tag{3.10a}$$

$$\frac{1}{\alpha}\partial_x = \mathcal{I} - \mathcal{L}_R = \mathcal{L}_R(\mathcal{L}_R^{-1} - \mathcal{I}) = -\mathcal{D}_R(\mathcal{I} - \mathcal{D}_R)^{-1} = -\sum_{p=1}^{\infty} \mathcal{D}_R^p, \tag{3.10b}$$

where $\mathcal{D}^p$ is successively defined as $\mathcal{D}^p = \mathcal{D}[\mathcal{D}^{p-1}]$. We will truncate the series (3.10) and only compute the corresponding partial sum to approximate the $A_x^{\pm}$ in (3.2)–(3.4). For stabilization of the high order form of the truncated Neumann series, we need to introduce the additional operator $\mathcal{D}_0$:

$$\mathcal{D}_0[v,a] = v(a) - \frac{\alpha}{2}\int_a^b e^{-\alpha|x-y|} v(y)dy - A_0 e^{-\alpha(x-a)} - B_0 e^{-\alpha(b-x)}, \tag{3.11}$$

where A_0 and B_0 are determined by boundary conditions. For example, if $\mathcal{D}_0$ is a periodic function such that

$$\mathcal{D}_0[v,\alpha](a) = \mathcal{D}_0[v,\alpha](b) \quad \text{and} \quad \partial_x\mathcal{D}_0[v,\alpha](a) = \partial_x\mathcal{D}_0[v,\alpha](b),$$

then we get

$$A_0 = \frac{I^0[v,\alpha](b)}{1-\mu} \quad B_0 = \frac{I_0[v,\alpha](a)}{1-\mu} \tag{3.12}$$

with $I^0[v,\alpha](x) = \frac{\alpha}{2}\int_a^b e^{-\alpha|x-y|}v(y)dy$. And, as before, if we require

$$\mathcal{D}_0[v,\alpha](a) = C_a \quad \text{and} \quad \mathcal{D}_0[v,\alpha](b) = C_b$$

with given numbers C_a and C_b, then the boundary coefficients are obtained as

$$A_0 = \frac{1}{1-\mu^2}\left(\mu\left(I^0[v,\alpha](b) - v(b) + C_b\right) - \left(I^0[v,\alpha](a) - v(a) + C_a\right)\right), \tag{3.13a}$$

$$B_0 = \frac{1}{1-\mu^2}\left(\mu\left(I^0[v,\alpha](a) - v(a) + C_a\right) - \left(I^0[v,\alpha](b) - v(b) + C_b\right)\right). \tag{3.13b}$$

In the following, we will study the properties of the partial sums with different boundary conditions. Additionally, we will discuss the parameter α and its role in ensuring accuracy and unconditional stability.

3.2.1. Periodic boundary conditions. If A is a periodic function, we define the approximations of the first derivatives $A_x^{\pm}$ using partial sums as

$$A_x^- \approx \mathcal{P}_k^-[A,\alpha](x) = \begin{cases} \alpha\sum_{p=1}^k \mathcal{D}_L^p[A,\alpha](x), & k=1,2, \\ \alpha\sum_{p=1}^k \mathcal{D}_L^p[A,\alpha](x) - \alpha\mathcal{D}_0 * \mathcal{D}_L^2[A,\alpha](x), & k=3, \end{cases} \tag{3.14a}$$

and

$$A_x^+ \approx \mathcal{P}_k^+[A,\alpha](x) = \begin{cases} -\alpha\sum_{p=1}^k \mathcal{D}_R^p[A,\alpha](x), & k=1,2, \\ -\alpha\sum_{p=1}^k \mathcal{D}_R^p[A,\alpha](x) + \alpha\mathcal{D}_0 * \mathcal{D}_R^2[A,\alpha](x), & k=3. \end{cases} \tag{3.14b}$$

Then, we have the following theorem, which gives an error estimate for the partial sums approximation and has been proven in [16].

THEOREM 3.1. *Suppose $v(x) \in C^{k+1}[a,b]$ is a periodic smooth function. Consider the operators D_* with the boundary treatment $\mathcal{D}_*(a) = \mathcal{D}_*(b)$. Here, $*$ can be L, R, and 0. Then,*

$$\|A_x - \mathcal{P}_k^-[A,\alpha]\|_\infty = \mathcal{O}\left(1/\alpha^k\right), \quad \|A_x - \mathcal{P}_k^+[A,\alpha]\|_\infty = \mathcal{O}\left(1/\alpha^k\right). \tag{3.15}$$

Here, we take $\alpha = \beta/(c\Delta t)$, where c is the maximum wave speed and β is a constant independent of the time step Δt. Therefore, the accuracy for the approximation (3.14) to the $\partial_x A$ is $\mathcal{O}(\Delta t^k)$. Note that, to achieve kth order accuracy in time, $k = 1,2,3$, we should employ the kth order SSP RK method (3.2)–(3.4) as well as $\mathcal{P}_k^{\pm}$ in (3.14). Moreover, if β is chosen appropriately, the semidiscrete scheme (without numerical approach to $\mathcal{D}^p$) is A-stable and hence allows for large time step evolution. Additionally, the linear stability of the method, outlined in the following theorem, has been proven in [16].

TABLE 3.1
$\beta_{k,\max}$ in Theorem 3.2 for $k = 1, 2, 3$.

k	1	2	3
$\beta_{k,max}$	2	1	1.243

THEOREM 3.2. *For the linear equation $\phi_t + c\phi_x = 0$, (i.e., the Hamiltonian is linear) with periodic boundary conditions, we consider the* kth *order SSP RK method as well as the* kth *partial sum in* (3.14) *with $\alpha = \beta/(|c|\Delta t)$. Then there exists a constant $\beta_{k,max} > 0$ for $k = 1, 2, 3$ such that the scheme is A-stable provided $0 < \beta \leq \beta_{k,\max}$. The constants $\beta_{k,max}$ for $k = 1, 2, 3$ are summarized in Table* 3.1.

Note that for $k = 3$, we modify the partial sum $\mathcal{P}_3^{\pm}$ with a extra term $\alpha\mathcal{D}_0 * \mathcal{D}_*^2$, where $*$ can be L or R. This is because we found that the scheme coupling the partial sum, $\alpha\sum_{p=1}^{3}\mathcal{D}_L^p[A,\alpha](x)$ or $-\alpha\sum_{p=1}^{3}\mathcal{D}_R^p[A,\alpha](x)$, with third order SSP RK method could not maintain the A-stable property. In fact, $-\alpha^2\mathcal{D}_0[v,\alpha]$ is an approximation to v_{xx}, which has been proven in [17]. Therefore, the extra terms $\alpha\mathcal{D}_0 * \mathcal{D}_*^2$ in (3.14) are approximations to $(1/\alpha^3)\partial_x^4 A$ and hence help enhance the stability of our scheme by adding extra fourth order numerical dissipation.

3.2.2. Outflow boundary conditions. In this section we will address outflow boundary conditions. We will cast the needed data in terms of a general condition which is discussed in [17]. To achieve a higher order accuracy for the nonperiodic case, we need a modification of the partial sums (3.14). For nonperiodic boundary conditions, this additional information is needed at the boundaries. This additional information takes the form of derivative values at the boundary, i.e., $\partial_x^m A(a)$ and $\partial_x^m A(b)$, $m \geq 1$. For now assume we have this data, but later in this sections we will summarize an approach for constructing this data for outflow. Using integration by parts one can derive the following modified partial sums for $k \leq 3$ to deal with the nonperiodic boundary conditions:

$$\text{(3.16a)}\quad A_x^- \approx \widetilde{\mathcal{P}}_k^-[A,\alpha](x) = \begin{cases} \alpha\displaystyle\sum_{p=1}^{k}\mathcal{D}_L[A_{1,p},\alpha](x), & k = 1, 2, \\ \alpha\displaystyle\sum_{p=1}^{k}\mathcal{D}_L[A_{1,p},\alpha](x) - \alpha\mathcal{D}_0[A_{1,3},\alpha](x), & k = 3, \end{cases}$$

(3.16b)

$$A_x^+ \approx \widetilde{\mathcal{P}}_k^+[A,\alpha](x) = \begin{cases} -\alpha\displaystyle\sum_{p=1}^{k}\mathcal{D}_R[A_{2,p},\alpha](x), & k = 1, 2, \\ -\alpha\displaystyle\sum_{p=1}^{k}\mathcal{D}_R[A_{2,p},\alpha](x) + \alpha\mathcal{D}_0[A_{2,3},\alpha](x), & k = 3. \end{cases}$$

And $A_{1,p}$ and $A_{2,p}$ are given as

$$\text{(3.17a)}\qquad \begin{cases} A_{1,1} = A, \\ A_{1,2} = \mathcal{D}_L[A_{1,1},\alpha] - \displaystyle\sum_{m=2}^{k}\left(-\frac{1}{\alpha}\right)^m \partial_x^m A(a)e^{-\alpha(x-a)}, \\ A_{1,3} = \mathcal{D}_L[A_{1,2},\alpha] + \displaystyle\sum_{m=2}^{k}(m-1)\left(-\frac{1}{\alpha}\right)^m \partial_x^m A(a)e^{-\alpha(x-a)}, \end{cases}$$

$$\text{(3.17b)}\qquad \begin{cases} A_{2,1} = A, \\ A_{2,2} = \mathcal{D}_R[A_{2,1},\alpha] - \displaystyle\sum_{m=2}^{k} \left(\frac{1}{\alpha}\right)^m \partial_x^m A(b) e^{-\alpha(b-x)}, \\ A_{2,3} = \mathcal{D}_R[A_{2,2},\alpha] + \displaystyle\sum_{m=2}^{k} (m-1) \left(\frac{1}{\alpha}\right)^m \partial_x^m A(b) e^{-\alpha(b-x)}, \end{cases}$$

where the boundary conditions for the operators are imposed as

$$\begin{aligned} &\alpha\mathcal{D}_L[A_{1,1},\alpha](a) = A_x(a), \quad \alpha\mathcal{D}_R[A_{2,1},\alpha](b) = -A_x(b), \\ &\alpha\mathcal{D}_L[A_{1,p},\alpha](a) = \alpha\mathcal{D}_R[A_{2,p},\alpha](b) = 0 \quad \text{for } p \geq 2, \\ &\alpha\mathcal{D}_0[A_{*,3},\alpha](a) = \alpha\mathcal{D}_0[A_{*,3},\alpha](b) = 0, \quad * \text{ could be 1 or 2.} \end{aligned}$$

Then, the modified partial sum (3.16) agrees with the derivative values at the boundary:

$$\widetilde{\mathcal{P}}_k^-[A,\alpha](a) = A_x(a), \quad \widetilde{\mathcal{P}}_k^+[A,\alpha](b) = A_x(b).$$

Furthermore, we have the following theorem, which is a result of the Theorem 2.3 from [17].

THEOREM 3.3. *Suppose* $A \in \mathcal{C}^{k+1}[a,b]$. *Then the modified partial sums* (3.16) *satisfy*

$$\text{(3.18)}\qquad \|A_x - \widetilde{\mathcal{P}}_k^-[A,\alpha]\|_\infty = \mathcal{O}(1/\alpha^k), \quad \|A_x - \widetilde{\mathcal{P}}_k^+[A,\alpha]\|_\infty = \mathcal{O}(1/\alpha^k), \quad k = 1,\, 2,\, 3.$$

Again, we take $\alpha = \beta/(c\Delta t)$, where c is the maximum wave speed and β is the same as in the case of the periodic boundary conditions; see Table 3.1.

As we have seen in (3.17), for high order we need the derivatives $\partial_x^m A(a)$ and $\partial_x^m A(b)$, $m \geq 1$, for nonperiodic boundary conditions. Here, we will only focus on the outflow boundary conditions. For outflow we construct the derivatives using high order extrapolation at boundaries (that is, there are no physical boundaries given). The details of the general nonperiodic conditions can be found in our previous work [17].

3.2.3. Space discretization. According to the kernel-based method, the spatial derivatives can be approximated by the partial sums based on an integral formulation. A fully discrete numerical solution is then obtained by discretizing $\mathcal{D}_L$ and $\mathcal{D}_R$ operators in space. In this subsection we will give the details of the spatial discretization of the $\mathcal{D}_L$ and $\mathcal{D}_R$ operators and the WENO-based quadrature formulation to approximate the convolution integrals appearing in the $\mathcal{D}_L$ and $\mathcal{D}_R$ operators.

Suppose we divide the domain $[a,b]$ with $N+1$ uniformly distributed grid points:

$$\Delta x = (b-a)/N, \quad x_i = a + i\Delta x, \quad i = 0, 1, \ldots, N.$$

The convolution integrals $I_i^L = I^L[v,\alpha](x_i)$ and $I_i^R = I^R[v,\alpha](x_i)$ satisfy a recursive relation:

$$\text{(3.19a)}\qquad I_i^L = e^{-\alpha\Delta x_i} I_{i-1}^L + J_i^L, \quad i = 1, \ldots, N, \quad I_0^L = 0,$$

$$\text{(3.19b)}\qquad I_i^R = e^{-\alpha\Delta x_{i+1}} I_{i+1}^R + J_i^R, \quad i = 0, \ldots, N-1, \quad I_N^R = 0,$$

where

$$J_i^L = \alpha \int_{x_{i-1}}^{x_i} v(y) e^{-\alpha(x_i - y)} dy, \quad J_i^R = \alpha \int_{x_i}^{x_{i+1}} v(y) e^{-\alpha(y - x_i)} dy. \tag{3.20}$$

Since there is a unique polynomial $p(x)$ of degree at most k that interpolates $v(x)$ at the nodes in the interpolation stencil $S(i) = \{x_{i-r}, \dots, x_{i-r+k}\}$, which contains x_{i-1} and x_i, we can approximate J_i^L with kth order accuracy by

$$J_i^L \approx \alpha \int_{x_{i-1}}^{x_i} p(y) e^{-\alpha(x_i - y)} dy. \tag{3.21}$$

Note that the integral on the right-hand side can be evaluated exactly. Similarly, J_i^R can be approximated by

$$J_i^R \approx \alpha \int_{x_i}^{x_{i+1}} p(y) e^{-\alpha(y - x_i)} dy \tag{3.22}$$

with polynomial $p(x)$ interpolating $v(x)$ on stencil $S(i) = \{x_{i+r-k}, \dots, x_{i+r}\}$, which includes x_i and x_{i+1}.

Since the quadratures with a fixed stencil for approximating the J_i^L and J_i^L may develop spurious oscillations which violate the entropy solutions, we will use WENO-based quadrature formula and the nonlinear filter to control oscillations and capture the correct solution, which is proposed in [17]. Here we will provide a brief description.

To summarize, if A_x is a periodic function, then we will be using the following modified sums framework instead of (3.14) for approximation of $A_x^{\pm}$ at x_i:

$$A_{x,i}^- = \alpha \mathcal{D}_L[A, \alpha](x_i) + \alpha \sum_{p=2}^{k} \sigma_{i,L}^{p-2} \mathcal{D}_L^p[A, \alpha](x_i), \tag{3.23a}$$

$$A_{x,i}^+ = -\alpha \mathcal{D}_R[A, \alpha](x_i) - \alpha \sum_{p=2}^{k} \sigma_{i,R}^{p-2} \mathcal{D}_R^p[A, \alpha](x_i), \tag{3.23b}$$

and if A_x is a nonperiodic function, then we we will use the following formulation instead of (3.16):

$$A_{x,i}^- = \alpha \mathcal{D}_L[A_{1,1}, \alpha](x_i) + \alpha \sum_{p=2}^{k} \sigma_{i,L}^{p-2} \mathcal{D}_L[A_{1,p}, \alpha](x_i), \tag{3.24a}$$

$$A_{x,i}^+ = -\alpha \mathcal{D}_R[A_{2,1}, \alpha](x_i) - \alpha \sum_{p=2}^{k} \sigma_{i,R}^{p-2} \mathcal{D}_R[A_{2,p}, \alpha](x_i). \tag{3.24b}$$

Moreover, we only use the WENO formulation when $p = 1$ and apply a cheap high order linear formulation (3.21) and (3.22) for the case $p > 1$. The filters $\sigma_{i,L}$ and $\sigma_{i,R}$ are obtained based on the smoothness indicators from the WENO quadrature.

The fifth order WENO quadrature for J_i^L is presented here as an example. The related stencil is given in Figure 3.1. We choose the big stencil as $S(i) = \{x_{i-3}, \dots, x_{i+2}\}$ and the three small stencils as $S_r(i) = \{x_{i-3+r}, \dots, x_{i+r}\}$, $r = 0, 1, 2$.

1. We approximate the integrals on each small stencils $S_r(i)$ as follows:

$$J_{i,r}^L = \alpha \int_{x_{i-1}}^{x_i} e^{-\alpha(x_i - y)} p_r(y) dx, = \sum_{j=0}^{3} c_j^{(r)} v_{i-3+r+j}, \tag{3.25}$$

where $p_r(x)$ is the polynomial interpolating $v(x)$ on nodes $S_r(i)$, and the coefficients $c_j^{(r)}$ depend on α and the cell size Δx but not on v.

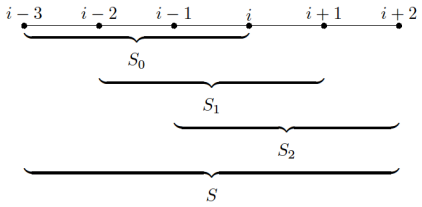

FIG. 3.1. *The structure of the stencils in WENO integration.*

2. Similarly, on the big stencil $S(i)$, we obtain

$$J_i^L = \alpha \int_{x_{i-1}}^{x_i} e^{-\alpha(x_i - y)} p(y) dx = \sum_{r=0}^{2} d_r J_{i,r}^L \tag{3.26}$$

with the linear weights d_r satisfying $\sum_{r=0}^{2} d_r = 1$.

3. We develop the following nonlinear weights ω_r using the linear weights d_r:

$$\omega_r = \tilde{\omega}_r / \sum_{s=0}^{2} \tilde{\omega}_s, \quad r = 0,\ 1,\ 2, \tag{3.27}$$

with

$$\tilde{\omega}_r = d_r \left(1 + \frac{\tau_5}{\epsilon + \beta_r} \right).$$

We take $\epsilon = 10^{-6}$ as a small positive number, $\epsilon > 0$, in our numerical test problems to avoid zero at the denominator. The smoothness indicator β_r is determined as

$$\beta_r = \sum_{l=2}^{3} \int_{x_{i-1}}^{x_i} \Delta x_i^{2l-3} \left(\frac{\partial^l p_r(x)}{\partial x^l} \right)^2 dx, \tag{3.28}$$

which is used to measure the relative smoothness of the function $v(x)$ in the stencil $S_r(i)$. Here, $\tau_5 = |\beta_0 - \beta_2|$. Furthermore, we introduce a parameter ξ_i as

$$\xi_i = \frac{\beta_{min}}{\beta_{max}}, \tag{3.29}$$

which will be use to create the nonlinear filter. Here,

$$\beta_{max} = 1 + \left(\frac{\tau_5}{\epsilon + \min(\beta_0, \beta_2)} \right)^2, \quad \beta_{min} = 1 + \left(\frac{\tau_5}{\epsilon + \max(\beta_0, \beta_2)} \right)^2.$$

Note that we have developed the nonlinear weights using the idea of the WENO-Z method proposed in [8], which has less dissipation and higher resolution compared to the original WENO method.

4. Lastly, we obtain the approximation

$$J_i^L = \sum_{r=0}^{2} \omega_r J_{i,r}^L. \tag{3.31}$$

The filter $\sigma_{i,L}$ is determined as

$$\sigma_{i,L} = \min(\xi_{i-1}, \xi_i). \tag{3.32}$$

All coefficients are given in Appendix A. The process to obtain J_i^R and $\sigma_{i,R}$ is mirror symmetric to that of J_i^L and $\sigma_{i,L}$ with respect to point x_i.

To close this section, we summarize the proposed method for approximating 1D problem (3.1) in the following algorithm flowchart.

Given the function u^n, the approximation order $k \leq 3$, the mesh size Δx, and the time step Δt

---

1. Choose β from Table 3.1. Compute $c = \max|H'(\phi)|$ at time t^n.
2. On each inner stage of the kth order SSP RK scheme do the following:
   (a) Compute c, and then obtain parameters $\alpha = \beta/(c\Delta t)$. For nonperiodic boundary conditions, compute the derivatives $\partial_x^m A(a)$ and $\partial_x^m A(b)$, $m = 1, \ldots, k$.
   (b) Apply $\mathcal{D}_L$ and $\mathcal{D}_R$ on A, respectively. Use the WENO quadrature to calculate $J^{L,R}$ and at the same time obtain the nonlinear filter $\sigma_{L,R}$. Compute $I^{L,R}$ via (3.19) and then calculate the parameter A_L, and B_R based on the boundary condition. Combine $I^{L,R}$, A_L, and B_R to construct $\mathcal{D}_L[A]$ and $\mathcal{D}_R[A]$.
   (c) For $k > 1$, also construct $\mathcal{D}_L^p[A] = \mathcal{D}_L^{p-1}[\mathcal{D}_L[A]]$ and $\mathcal{D}_R^p[A] = \mathcal{D}_R^{p-1}[\mathcal{D}_R[A]]$, or the modified funtions $\mathcal{D}^{L,R}[A_{1,2,k}]$ in (3.17), by a similar procedure for $1 < p \leq k$. WENO quadrature is not needed for construction of these high order terms.
   (d) Construct $A_x^{\pm}$ based on the the partial sum approximations (3.14) or (3.16).
   (e) Substitute into the Lax–Friedrichs Hamiltonian flux (3.5) and update the solution accordingly.

3.3. 2D magnetic potential equation. According to the CT formulation described in section 2.1, we must update the solution of the magnetic potential equation by solving a discrete version of the following equation:

$$A_t^3 + u^1(x,y)A_x^3 + u^2(x,y)A_y^3 = 0, \tag{3.33}$$

where the velocity components u^1 and u^2 are known from the previous time step due to the solution of the base part. Since the velocity functions are given, we can consider (3.33) as an HJ equation

$$A_t^3 + H(A_x^3, A_y^3) = 0 \tag{3.34}$$

with Hamiltonian flux

$$H(A_x^3, A_y^3) = u^1(x,y)A_x^3 + u^2(x,y)A_y^3. \tag{3.35}$$

We can directly apply a 2D version of the framework presented in section 3.1. The 2D semidiscrete scheme can be written as

$$\frac{dA_{i,j}^3(t)}{dt} = -\hat{H}(A_x^{3-}|_{i,j}, A_x^{3+}|_{i,j}, A_y^{3-}|_{i,j}, A_y^{3+}|_{i,j}) \tag{3.36}$$

at each point (x_i, y_j), where $\hat{H}$ is a Lipschitz continuous Hamiltonian flux. If we use the global Lax–Friedrichs flux, (3.36) becomes

$$\begin{aligned}\frac{dA^3_{i,j}(t)}{dt} =& - u^1_{i,j}\Big(\frac{A^{3-}_x + A^{3+}_x}{2}\Big)|_{i,j} - u^2_{i,j}\Big(\frac{A^{3-}_y + A^{3+}_y}{2}\Big)|_{i,j} \\ &+ c_1\Big(\frac{A^{3+}_x - A^{3-}_x}{2}\Big)|_{i,j} + c_2\Big(\frac{A^{3+}_y - A^{3-}_y}{2}\Big)|_{i,j}\end{aligned} \tag{3.37}$$

with

$$c_1 = \max_{i,j} |u^1_{i,j}| \quad \text{and} \quad c_2 = \max_{i,j} |u^2_{i,j}|.$$

We remark that the scheme (3.37) with global wave speeds can be very dissipative for some HJ equations. Instead, we can use the localized version of the Lax–Friedrichs flux, in which the maximum is computed over local states.

The approximations $A^{3\pm}_x|_{i,j}$ and $A^{3\pm}_y|_{i,j}$ to the derivatives of functions $A_x(x, y)$ and $A_y(x, y)$ at (x_i, y_j), respectively, are being calculated directly using 1D formulation of the scheme, e.g., when computing $A^{3\pm}_x$, we fix y and apply 1D scheme in x-direction. For example, when A_x is periodic in x-direction, we get

$$\begin{aligned}A^-_x &\approx \alpha_1 \mathcal{D}^p_L[A(\cdot, y), \alpha_1](x) + \alpha_1 \sum_{p=2}^{k} \sigma^{p-2}_{i,L} \mathcal{D}^p_L[A(\cdot, y), \alpha_1](x), \\ A^+_x &\approx -\alpha_1 \mathcal{D}_R[A(\cdot, y), \alpha_1](x) - \alpha_1 \sum_{p=2}^{k} \sigma^{p-2}_{i,R} \mathcal{D}^p_R[A(\cdot, y), \alpha_1](x).\end{aligned}$$

Here, we choose $\alpha_1 = \beta/(c_1\Delta t)$. Similarly, to approximate $A^{\pm}_y$, we fix x and obtain

$$\begin{aligned}A^-_y &\approx \alpha_2 \mathcal{D}_L[A(x, \cdot), \alpha_2](y) + \alpha_2 \sum_{p=2}^{k} \sigma^{p-2}_{i,L} \mathcal{D}^p_L[A(x, \cdot), \alpha_2](y), \\ A^+_y &\approx -\alpha_2 \mathcal{D}_R[A(x, \cdot), \alpha_2](y) - \alpha_2 \sum_{p=2}^{k} \sigma^{p-2}_{i,R} \mathcal{D}^p_R[A(x, \cdot), \alpha_2](y)\end{aligned}$$

with $\alpha_2 = \beta/(c_2\Delta t)$. Note that in the 2D case, we need to choose β_{max} as half of that for the 1D case to ensure the unconditional stability of the scheme.

In the case of nonperiodic boundary conditions, we still use extrapolation with suitable order of accuracy for the derivative values at an outflow boundary, as in the 1D formulation. For the details, see [17].

3.4. 3D magnetic potential equation. Although the evolution equation for the 3D magnetic potential (2.8) is significantly different from the evolution equation for the 2D scalar magnetic potential (3.33), we can still directly apply the scheme presented in section (3.1) to the 3D case. Writing out the magnetic vector potential equation derived in section (2.2) in component form we have

$$\partial_t A^1 = u^2(\partial_x A^2) + u^3(\partial_x A^3) - u^2(\partial_y A^1) - u^3(\partial_z A^1), \tag{3.38}$$

$$\partial_t A^2 = -u^1(\partial_x A^2) + u^1(\partial_y A^1) + u^3(\partial_y A^3) - u^3(\partial_z A^2), \tag{3.39}$$

$$\partial_t A^3 = -u^1(\partial_x A^3) - u^2(\partial_y A^3) + u^1(\partial_z A^1) + u^2(\partial_z A^2) \tag{3.40}$$

with $\mathbf{A} = (A^1, A^2, A^3)$ and $\mathbf{u} = (u^1, u^2, u^3)$. While $\mathbf{A}$ in three dimensions is not strictly an HJ equation, with the new implicit approach, we can simply apply the ideas from the 2D case. Then we can obtain the following equations using the Lax–Friedrichs flux splitting:

$$\begin{aligned}\frac{dA^1(t)}{dt} = \;& u^2\frac{(A_x^{2+}+A_x^{2-})}{2} - c_2\frac{(A_x^{2-}-A_x^{2+})}{2} + u^3\frac{(A_x^{3+}+A_x^{3-})}{2} - c_3\frac{(A_x^{3-}-A_x^{3+})}{2}\\ &- u^2\frac{(A_y^{1+}+A_y^{1-})}{2} - c_2\frac{(A_y^{1-}-A_y^{1+})}{2} - u^3\frac{(A_z^{1+}+A_z^{1-})}{2} - c_3\frac{(A_z^{1-}-A_z^{1+})}{2}, \qquad (3.41a)\\ \frac{dA^2(t)}{dt} = \;& - u^1\frac{(A_x^{2+}+A_x^{2-})}{2} - c_1\frac{(A_x^{2-}-A_x^{2+})}{2} + u^1\frac{(A_y^{1+}+A_y^{1-})}{2} - c_1\frac{(A_y^{1-}-A_y^{1+})}{2}\\ &+ u^3\frac{(A_y^{3+}+A_y^{3-})}{2} - c_3\frac{(A_y^{3-}-A_y^{3+})}{2} - u^3\frac{(A_z^{2+}+A_z^{2-})}{2} - c_3\frac{(A_z^{2-}-A_z^{2+})}{2}, \qquad (3.41b)\\ \frac{dA^3(t)}{dt} = \;& - u^1\frac{(A_x^{3+}+A_x^{3-})}{2} - c_1\frac{(A_x^{3-}-A_x^{3+})}{2} - u^2\frac{(A_y^{3+}+A_y^{3-})}{2} - c_2\frac{(A_y^{3-}-A_y^{3+})}{2}\\ &+ u^1\frac{(A_z^{1+}+A_z^{1-})}{2} - c_1\frac{(A_z^{1-}-A_z^{1+})}{2} + u^2\frac{(A_z^{2+}+A_z^{2-})}{2} - c_2\frac{(A_z^{2-}-A_z^{2+})}{2} \qquad (3.41c)\end{aligned}$$

at (x_i, y_j, z_k), where

$$c_1 = \max_{i,j,k}|u^1_{i,j,k}|, \quad c_2 = \max_{i,j,k}|u^2_{i,j,k}|, \quad \text{and} \quad c_3 = \max_{i,j,k}|u^3_{i,j,k}|.$$

Similarly, we use the 1D kernel-based formulation to approximate the derivatives of the magnetic vector potential components $A_x^{*\pm}$, $A_y^{*\pm}$, and $A_z^{*\pm}$, where $*$ denotes $1, 2$, and 3. In addition, since the density or pressure may become negative in some problems such as the blast wave problem, we use the positivity preserving limiter idea developed in our previous work [20], which is fully described in [18, 19, 44].

3.5. The cost of the MOL$^{\mathrm{T}}$ algorithm. The cost of the method is $O(N)$ [10, 13, 11, 12, 15]. Due to our fast summation method [11], using the first order form of the update for $\mathbf{A}$ with the proposed approach in the stages of third order RK is literally no more expensive than the standard WENO method for the vector potential in [20]. However, to be third order in time, at each stage value of the RK method, we do 3 convolution operator corrections to give third order in time, which means that the update for $\mathbf{A}$ is 3 times the cost of the old method in [20] for the update of $\mathbf{A}$. There are two points to make here. First, the new method has an A-stable property which eliminates the need for the additional diffusive limiters in the magnetic potential equation [20]. This is important for strong shocks, as will be discussed in the next section. Second, a possible solution to the above concern is to do a single step version of the method based on Adams–Bashforth (AB) and it could solve the issue of cost. Using von Neumann analysis, it is easy to show that for a linear HJ equation, AB combined with MOL$^{\mathrm{T}}$ leads to an unconditionally stable method. Hence, if cutting cost of the method is a priority, a straightforward line of research would be to replace the RK update for $\mathbf{A}$ by a single step AB method and cut the cost of computing $\mathbf{A}$ by a factor of 3. We have developed such an AB-MOL$^{\mathrm{T}}$ approach in one dimensions and this line of work is part of our future efforts.

4. Numerical results. In this section, we present the numerical results to demonstrate the accuracy and efficiency of the new method. We use the third order SSP RK method for the time discretization. Time step is chosen as

$$\Delta t = \frac{\text{CFL}}{em * cd}, \tag{4.1}$$

where the CFL number is 0.5, $em = \max(\lambda^5, \lambda^6)$, $cd = \frac{1}{\Delta x} + \frac{1}{\Delta y}$ for two dimensions and $cd = \frac{1}{\Delta x} + \frac{1}{\Delta y} + \frac{1}{\Delta z}$ for three dimensions.

4.1. Smooth vortex test in MHD. We first test the smooth vortex problem in two dimensions with a nonzero magnetic field to show the accuracy of the method within the CT formulation. The initial conditions are

$$(\rho, u^1, u^3, u^3, p, B^1, B^2, B^3) = (1, 1, 1, 0, 1, 0, 0, 0)$$

with perturbations on u^1, u^2, B^1, B^2, and p as

$$\begin{aligned}
(\delta u^1, \delta u^2) &= \frac{\mu}{2\pi} e^{0.5(1-r^2)}(-y, x), \\
(\delta B^1, \delta B^2) &= \frac{\kappa}{2\pi} e^{0.5(1-r^2)}(-y, x), \\
\delta p &= \frac{\mu^y (1-r^2) - \kappa^2}{8\pi^2} e^{(1-r^2)}.
\end{aligned}$$

And the initial condition for magnetic potential is

$$A^3(0, x, y) = \frac{\mu}{2\pi} e^{0.5(1-r^2)},$$

where $r^2 = x^2 + y^2$. The vortex strength is taken as $\mu = 5.389489439$ and $\kappa = \sqrt{2}\mu$ such that the lowest pressure is around 5.3×10^{-12} which happens in the center of the vortex. The domain is $[-10, 10] \times [-10, 10]$, and periodic boundary conditions are imposed. In Table 4.1, we present the errors of $\mathbf{B}$ at $t = 0.05$ with the mesh size 160×160. We observe fourth order accuracy in space for $\mathbf{B}$. Note that we use the fifth order WENO scheme for the solution of $\mathbf{A}$, but since we take the derivative of the magnetic potential equation to get the magnetic field, we lose an order of accuracy for $\mathbf{B}$; thus we get fourth order in space.

4.2. 2D Orszag–Tang vortex. The Orszang–Tang vortex problem is a standard model problem for testing $\nabla \cdot \mathbf{B} = 0$ condition, since the solution of the problem is sensitive to divergence errors at late times. The initial conditions are given as

$$(\rho, u^1, u^2, u^3, p, B^1, B^2, B^3) = (\gamma^2, -\sin(y), \sin(x), 0, \gamma, -\sin(y), \sin(2x), 0),$$

where $\gamma = 5/3$ is the ideal gas constant and the initial magnetic potential is

$$A^3 = 0.5\cos(2x) + \cos(y).$$

TABLE 4.1
Smooth vortex problem. Errors of $\mathbf{B}$ *and orders of accuracy.*

$N_x \times N_y$	L_1 error	Order	L_∞ error	Order
20×20	2.827E-03	–	1.479E-01	–
40×40	2.982E-04	3.245	1.839E-02	3.007
80×80	1.861E-05	4.003	1.327E-03	3.793
160×160	1.102E-06	4.078	1.126E-04	3.559
320×320	7.260E-08	3.924	1.170E-05	3.267

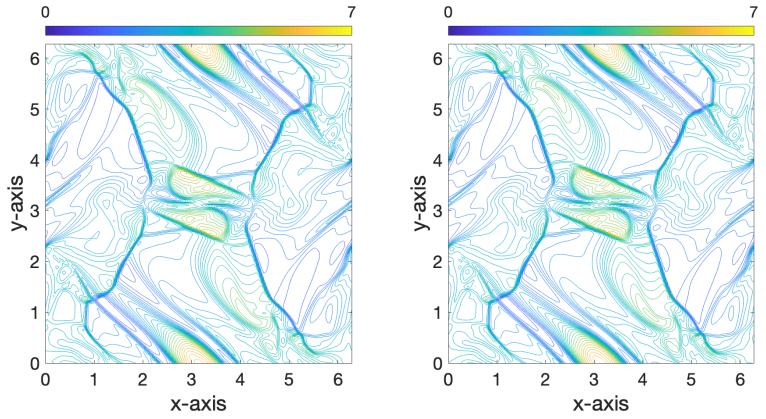

(a) Kernel-based method. (b) Previous method [20].

FIG. 4.1. *Orszag–Tang vortex problem. Contour plots of density at* $t = 3$ *with* 192×192 *grid points.*

The computational domain is $[0, 2\pi] \times [0, 2\pi]$, and periodic boundary conditions are used everywhere. We test the schemes with 192×192 grid points. Although the problem has a smooth initial condition, the solution generates an increasingly finer vortex structure throughout the domain as time progresses, rapidly dropping below the resolution of the mesh. In Figure 4.1, we show density ρ at time $t = 3$ and compare the results with our previous method [20]. We can see that they are in good agreement.

4.3. Cloud shock. In this section we consider the 2D cloud shock interaction problem, which models a strong shock passing through a dense stationary bubble. The initial conditions include

$$(\rho, u^1, u^2, u^3, p, B^1, B^2, B^3) = \begin{cases} (3.86859, 11.2536, 0, 0, 167.345, 0, 2.1826182, -2.1826182), & x < 0.05, \\ (1, 0, 0, 0, 1, 0, 0.56418958, 0.56418958), & x > 0.05, \end{cases}$$

and a circular cloud of density $\rho = 10$ and radius $r = 0.15$ centered at $(x, y) = (0.25, 0.5)$. The computational domain is $[0, 1] \times [0, 1]$ with mesh 512×512. We use an inflow boundary condition at left boundary and the high order outflow boundary condition elsewhere else. The initial condition for magnetic potential is

$$A^3 = \begin{cases} -2.1826182(x - 0.05), & x \le 0.05, \\ -0.56418958(x - 0.005), & x \ge 0.05\ . \end{cases}$$

Figure 4.2 presents Schlieren plots of $||\mathbf{B}||$ at $t = 0.06$. The new method matches well with our numerical results of our previous method [20].

4.4. 3D field loop. We tested an advecting field loop which moved diagonally across the boundary with an arbitrary initial angle. The initial conditions are

$$(\rho, u^1, u^2, u^3, p) = (1, 2/\sqrt{6}, 1/\sqrt{6}, 1/\sqrt{6}, 1).$$

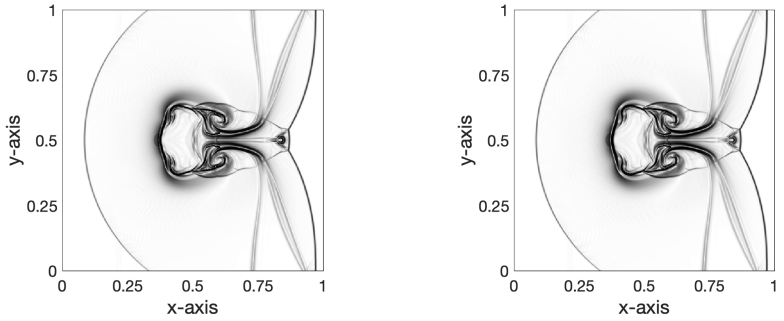

(a) Kernel-based method. (b) Previous method [20].

FIG. 4.2. *Cloud shock problem. Contour plots of* $\|\mathbf{B}\|$ *at* $t = 0.06$ *with* 512×512 *grid points.*

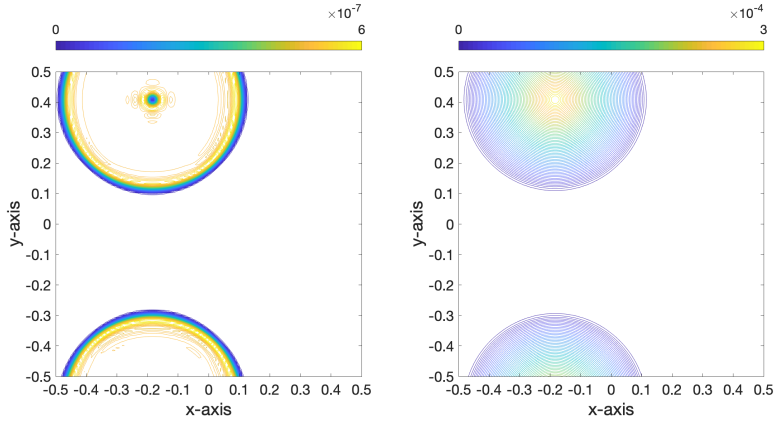

(a) $\|\mathbf{B}\|$ (b) $\mathbf{A}$

FIG. 4.3. *3D Field loop. Contour plots at time* $t = 1$ *with* 128×128 *grid points. The loop has been advected around the grid once.* (a) *Magnetic pressure;* (b) *magnetic potential.*

The initial conditions for magnetic field are determined by taking the curl of the magnetic potential, which is given as magnetic potential:

$$A^3 = \begin{cases} 0.001(R - r), & r \le R, \\ 0 & \text{otherwise}, \end{cases}$$

where $A^1 = 0$, $A^2 = 0$, and $r = \sqrt{x^2 + y^2}$ and $R = 0.3$. We use a domain size $[-0.5, 0.5] \times [-0.5, 0.5] \times [-0.5, 0.5]$ with $128 \times 128 \times 128$ mesh. Periodic boundary conditions are applied to all sides. We observe that the field loop integrity is maintained, after advecting diagonally around the domain, until the final time, $t = 1$. The results shown in Figure 4.3 are a 2D slice of the 3D solution taken at $z = 0$.

4.5. 3D blast wave. In this section we investigate the 3D version of the blast wave problem to show the strength of the new method, which eliminates the need for the diffusion limiter. The initial conditions are

$$(\rho, u^1, u^2, u^3, B^1, B^2, B^3) = (1, 0, 0, 0, 50/\sqrt{2\pi}, 50/\sqrt{2\pi}, 0)$$

with a spherical pressure pulse

$$p = \begin{cases} 1000, & r \le 0.1, \\ 0.1 & \text{otherwise.} \end{cases}$$

where $r = \sqrt{x^2 + y^2 + z^2}$. The initial condition for magnetic potential is

$$\mathbf{A}(0, x, y, z) = (0, 0, 50/\sqrt{2\pi}y - 50/\sqrt{2\pi}x).$$

We use a domain size $[-0.5, 0.5] \times [-0.5, 0.5] \times [-0.5, 0.5]$ with $150 \times 150 \times 150$ mesh. Outflow boundary conditions are applied everywhere.The results presented in Figure 4.4 and Figure 4.5 are the solutions cut at $z = 0$. The subplots highlight the differences between the two methods. The key differences are that the new method

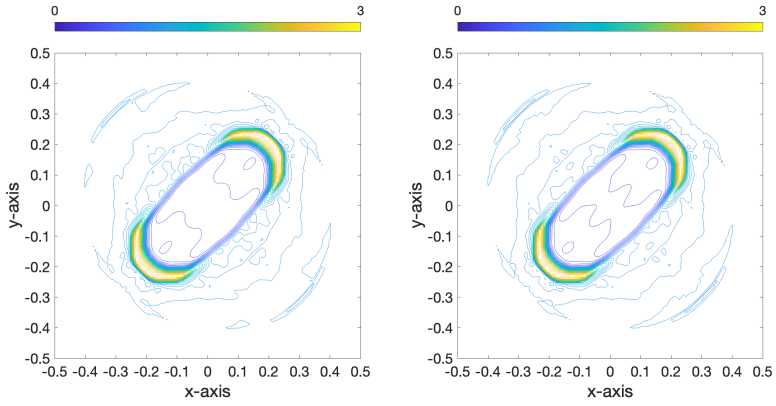

(a) Density with kernel-based method (b) Density with previous method [20]

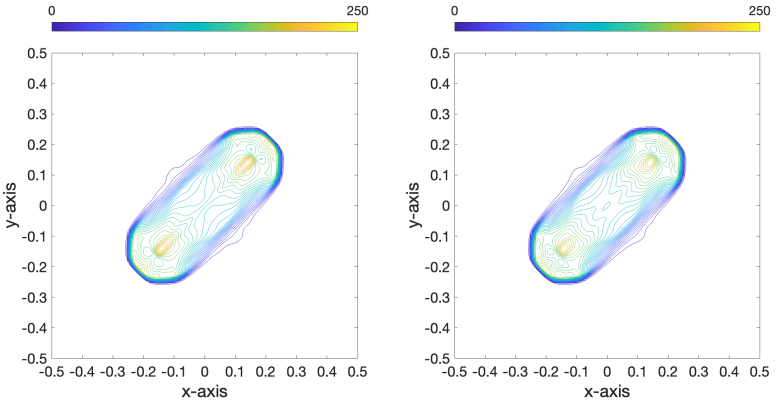

(c) Pressure with kernel-based method (d) Pressure with previous method [20]

FIG. 4.4. *3D blast wave problem. Contour plots at time* $t = 0.01$ *with* 150×150 *grid points.*

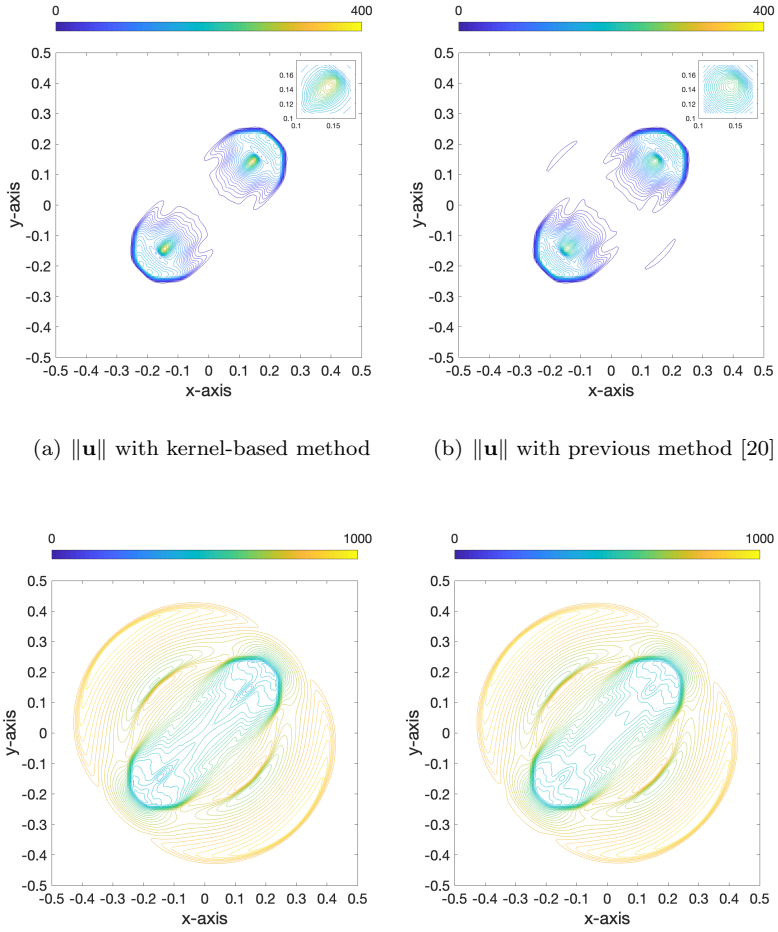

(a) $\|\mathbf{u}\|$ with kernel-based method (b) $\|\mathbf{u}\|$ with previous method [20]

(c) $\|\mathbf{B}\|$ with kernel-based method (d) $\|\mathbf{B}\|$ with previous method [20]

FIG. 4.5. *3D blast wave problem. Contour plots at time* $t = 0.01$ *with* 150×150 *grid points. While the max* $\|\mathbf{u}\|$ *value for the previous method is* 261*, it is* 320 *for the kernel-based method. Note that this is* 23% *higher than the old method and is far less isotropic around the peak than the old method.*

has a maximum value that achieves a peak of 320, which is 23% higher than the old method, and is far less isotropic around the peak than the old method. As demonstrated in a latter test, the isotropic behavior and lower peak in the strong blast wave are due to the diffusion limiter that was needed with the old explicit CT method.

4.6. Kernel-based method with diffusion terms. In this section we demonstrate the advantage of the new approach in the context of strong shocks. In the previous approach [20], we needed to add in a diffusion limiter to stabilize the update for $\mathbf{A}$ in the vicinity of a sharp change in the solution. This had no impact on smooth solutions and minimal impact on problems like the cloud shock. But in the context of the blast wave problem, while the diffusion limiter stabilized the solution, comparing $\|\mathbf{u}\|$ for both schemes, we have that the maximum value of the previous method is 261, while it is 320 for the kernel-based method. This involved decreasing

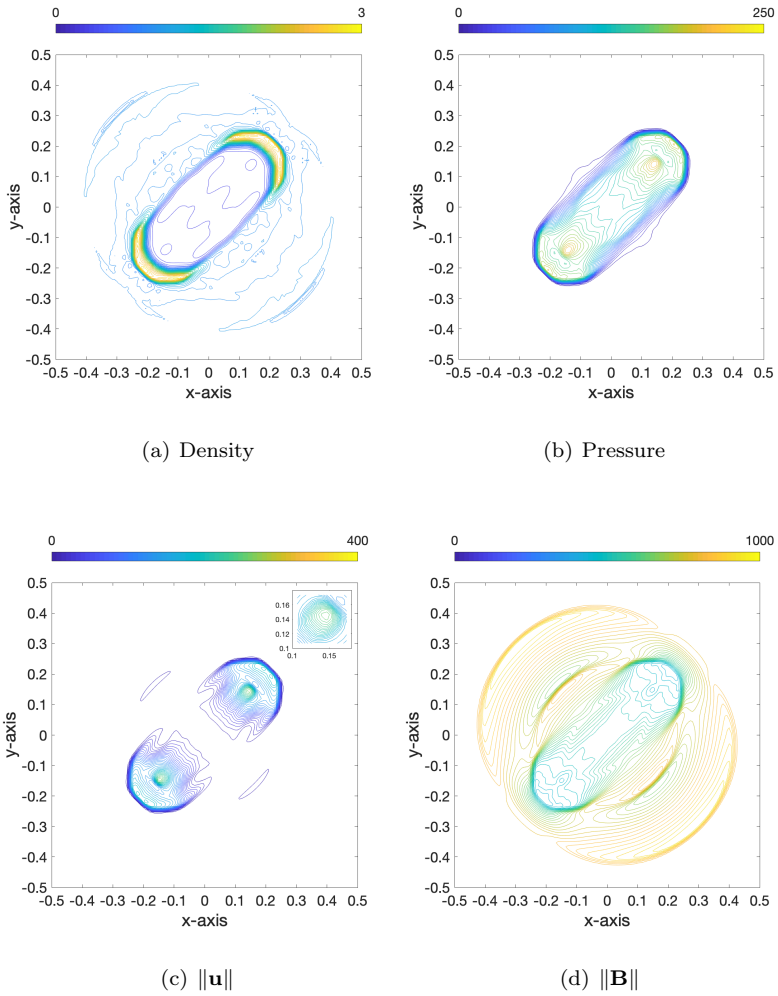

(a) Density (b) Pressure

(c) $\|\mathbf{u}\|$ (d) $\|\mathbf{B}\|$

FIG. 4.6. *3D blast wave from the kernel-based method after adding the diffusion limiter. The max* $\|\mathbf{u}\|$ *value is* 265. *We note that these results are nearly identical to the old WENO-HJ method, which required the diffusion limiter.*

the maximum values, making the solution more isotropic, and changing the structure of the contours away from the blast. In Figure 4.6, we show the solution generated by the new method with the diffusion limiter used in our previous code. In this case, the maximum value of $\|\mathbf{u}\|$ is 265. These results confirm that the limiter is what is causing a change in the solution structure for problems with strong shocks. Adding the diffusion limiter caused the solution to revert from the results of the new method to those obtained by the old method.

5. Conclusion. In this work we developed a kernel-based CT scheme based on the magnetic vector potential equations in two and three dimensions for ensuring that the solution of the magnetic field in ideal MHD is divergence-free. The development of the method relies on a kernel-based formulation of the spatial derivatives. The framework of the current method is derived from the MOL$^{\mathrm{T}}$ methodology and the key idea of successive convolution. The method relies on the idea of replacing a local

operator with an $O(N)$ global operator that is as efficient as an explicit method. Because the approximation is global, it provides a method that behaves unconditionally stable for HJ equations when coupled with explicit time stepping. For time integration, we coupled the method with explicit SSP RK schemes. The most important conclusion of this work is that the newly proposed method offers an approach to CT that is mesh aligned for AMR and does not rely on a diffusion limiter for stability in three dimensions, which we needed in our previous work [20]. This modification considerably improves solutions where there are strong shocks and, as demonstrated in numerical simulations, also works well for smooth problems. The method is robust and has been tested on a range of 2D and 3D test problems, such as the field loop and blast wave problems.

Appendix A. Formulation of WENO quadrature. Here, we show all coefficients in WENO quadrature. We denote $\nu = \alpha\Delta x$; then we have

$$
\begin{aligned}
c_0^{(0)} =& \frac{6-6\nu+2\nu^2-(6-\nu^2)e^{-\nu}}{6\nu^3},\\
c_1^{(0)} =& -\frac{6-8\nu+3\nu^2-(6-2\nu-2\nu^2)e^{-\nu}}{2\nu^3},\\
c_2^{(0)} =& \frac{6-10\nu+6\nu^2-(6-4\nu-\nu^2+2\nu^3)e^{-\nu}}{2\nu^3},\\
c_3^{(0)} =& -\frac{6-12\nu+11\nu^2-6\nu^3-(6-6\nu+2\nu^2)e^{-\nu}}{6\nu^3},\\
c_0^{(1)} =& \frac{6-\nu^2-(6+6\nu+2\nu^2)e^{-\nu}}{6\nu^3},\\
c_1^{(1)} =& -\frac{6-2\nu-2\nu^2-(6+4\nu-\nu^2-2\nu^3)e^{-nu}}{2\nu^3},\\
c_2^{(1)} =& \frac{6-4\nu-\nu^2+2\nu^3-(6+2\nu-2\nu^2)e^{-\nu}}{2\nu^3},\\
c_3^{(1)} =& -\frac{6-6\nu+2\nu^2-(6-\nu^2)e^{-\nu}}{6\nu^3},\\
c_0^{(2)} =& \frac{6+6\nu+2\nu^2-(6+12\nu+11\nu^2+6\nu^3)e^{-\nu}}{6\nu^3},\\
c_1^{(2)} =& -\frac{6+4\nu-\nu^2-2\nu^3-(6+10\nu+6\nu^2)e^{-\nu}}{2\nu^3},\\
c_2^{(2)} =& \frac{6+2\nu-2\nu^2-(6+8\nu+3\nu^2)e^{-\nu}}{2\nu^3},\\
c_3^{(2)} =& -\frac{6-\nu^2-(6+6\nu+2\nu^2)e^{-\nu}}{6\nu^3}.
\end{aligned}
$$

And the linear weights are

$$
\begin{aligned}
d_0 &= \frac{6-\nu^2-(6+6\nu+2\nu^2)e^{-\nu}}{3\nu((2-\nu)-(2+\nu)e^{-\nu})},\\
d_2 &= \frac{60-60\nu+15\nu^2+5\nu^3-3\nu^4-(60-15\nu^2+2\nu^4)e^{-\nu}}{10\nu^2(6-\nu^2-(6+6\nu+2\nu^2)e^{-\nu})},\\
d_1 &= 1-d_0-d_2.
\end{aligned}
$$

The smoothness indicator β_r has the expressions as

$$\beta_0 = \frac{13}{12}(-v_{i-3} + 3v_{i-2} - 3v_{i-1} + v_i)^2 + \frac{1}{4}(v_{i-3} - 5v_{i-2} + 7v_{i-1} - 3v_i)^2,$$
$$\beta_1 = \frac{13}{12}(-v_{i-2} + 3v_{i-1} - 3v_i + v_{i+1})^2 + \frac{1}{4}(v_{i-2} - v_{i-1} - v_i + v_{i+1})^2,$$
$$\beta_2 = \frac{13}{12}(-v_{i-1} + 3v_i - 3v_{i+1} + v_{i+2})^2 + \frac{1}{4}(-3v_{i-1} + 7v_i - 5v_{i+1} + v_{i+2})^2.$$

REFERENCES

[1] D. S. Balsara, *Divergence-free adaptive mesh refinement for magnetohydrodynamics*, J. Comput. Phys., 174 (2001), pp. 614–648.

[2] D. S. Balsara, *Second-order-accurate schemes for magnetohydrodynamics with divergence-free reconstruction*, Astrophys. J. Suppl. Ser., 151 (2004), p. 149.

[3] D. S. Balsara, *Divergence-free reconstruction of magnetic fields and WENO schemes for magnetohydrodynamics*, J. Comput. Phys., 228 (2009), pp. 5040–5056.

[4] D. S. Balsara and J. Kim, *A comparison between divergence-cleaning and staggered-mesh formulations for numerical magnetohydrodynamics*, Astrophys. J., 602 (2004), p. 1079.

[5] D. S. Balsara, C. Meyer, M. Dumbser, H. Du, and Z. Xu, *Efficient implementation of ADER schemes for Euler and magnetohydrodynamical flows on structured meshes—speed comparisons with Runge–Kutta methods*, J. Comput. Phys., 235 (2013), pp. 934–969.

[6] D. S. Balsara, T. Rumpf, M. Dumbser, and C.-D. Munz, *Efficient, high accuracy ADER-WENO schemes for hydrodynamics and divergence-free magnetohydrodynamics*, J. Comput. Phys., 228 (2009), pp. 2480–2516.

[7] D. S. Balsara and D. S. Spicer, *A staggered mesh algorithm using high order Godunov fluxes to ensure solenoidal magnetic fields in magnetohydrodynamic simulations*, J. Comput. Phys., 149 (1999), pp. 270–292.

[8] R. Borges, M. Carmona, B. Costa, and W. S. Don, *An improved weighted essentially non-oscillatory scheme for hyperbolic conservation laws*, J. Comput. Phys., 227 (2008), pp. 3191–3211.

[9] M. F. Causley, A. J. Christlieb, Y. Guclu, and E. Wolf, *Method of Lines Transpose: A Fast Implicit Wave Propagator*, preprint, arXiv:1306.6902, 2013.

[10] M. Causley, A. Christlieb, B. Ong, and L. Van Groningen, *Method of lines transpose: An implicit solution to the wave equation*, Math. Comput., 83 (2014), pp. 2763–2786.

[11] M. Causley, A. Christlieb, and E. Wolf, *Method of lines transpose: An efficient unconditionally stable solver for wave propagation*, J. Sci. Comput., 70 (2017), pp. 896–921.

[12] M. F. Causley, H. Cho, A. J. Christlieb, and D. C. Seal, *Method of lines transpose: High order L-stable $\mathcal{O}(N)$ schemes for parabolic equations using successive convolution*, SIAM J. Numer. Anal., 54 (2016), pp. 1635–1652.

[13] M. F. Causley and A. J. Christlieb, *Higher order A-stable schemes for the wave equation using a successive convolution approach*, SIAM J. Numer. Anal., 52 (2014), pp. 220–235.

[14] Y. Cheng, F. Li, J. Qiu, and L. Xu, *Positivity-preserving DG and central DG methods for ideal MHD equations*, J. Comput. Phys., 238 (2013), pp. 255–280.

[15] A. Christlieb, W. Guo, and Y. Jiang, *A WENO-based method of lines transpose approach for Vlasov simulations*, J. Comput. Phys., 327 (2016), pp. 337–367.

[16] A. Christlieb, W. Guo, and Y. Jiang, *Kernel based high order "explicit" unconditionally stable scheme for nonlinear degenerate advection-diffusion equations*, J. Sci. Comput., 82 (2020), 52.

[17] A. Christlieb, W. Guo, and Y. Jiang, *A kernel based high order "explicit" unconditionally stable scheme for time dependent Hamilton–Jacobi equations*, J. Comput. Phys., 379 (2019), pp. 214–236.

[18] A. J. Christlieb, X. Feng, D. C. Seal, and Q. Tang, *A high-order positivity-preserving single-stage single-step method for the ideal magnetohydrodynamic equations*, J. Comput. Phys., 316 (2016), pp. 218–242.

[19] A. J. Christlieb, Y. Liu, Q. Tang, and Z. Xu, *Positivity-preserving finite difference weighted ENO schemes with constrained transport for ideal magnetohydrodynamic equations*, SIAM J. Sci. Comput., 37 (2015), pp. A1825–A1845.

[20] A. J. Christlieb, J. A. Rossmanith, and Q. Tang, *Finite difference weighted essentially non-oscillatory schemes with constrained transport for ideal magnetohydrodynamics*, J. Comput. Phys., 268 (2014), pp. 302–325.

[21] W. Dai and P. R. Woodward, *A simple finite difference scheme for multidimensional magnetohydrodynamical equations*, J. Comput. Phys., 142 (1998), pp. 331–369.

[22] H. De Sterck, *Multi-dimensional upwind constrained transport on unstructured grids for 'shallow water' magnetohydrodynamics*, in Proceedings of the 15th AIAA Computational Fluid Dynamics Conference, Anaheim, CA, 2001.
[23] A. Dedner, F. Kemm, D. Kröner, C.-D. Munz, T. Schnitzer, and M. Wesenberg, *Hyperbolic divergence cleaning for the MHD equations*, J. Comput. Phys., 175 (2002), pp. 645–673.
[24] C. R. DeVore, *Flux-corrected transport techniques for multidimensional compressible magnetohydrodynamics*, J. Comput. Phys., 92 (1991), pp. 142–160.
[25] E. Dorfi, *Numerical methods for astrophysical plasmas*, Comput. Phys. Commun., 43 (1986), pp. 1–15.
[26] C. R. Evans and J. F. Hawley, *Simulation of magnetohydrodynamic flows—A constrained transport method*, Astrophys. J., 332 (1988), pp. 659–677.
[27] M. Fey and M. Torrilhon, *A constrained transport upwind scheme for divergence-free advection*, in Hyperbolic Problems: Theory, Numerics, Applications, Springer, Cham, 2003, pp. 529–538.
[28] P. Fu, F. Li, and Y. Xu, *Globally divergence-free discontinuous Galerkin methods for ideal magnetohydrodynamic equations*, J. Sci. Comput., 77 (2018), pp. 1621–1659.
[29] S. Gottlieb, C.-W. Shu, and E. Tadmor, *Strong stability-preserving high-order time discretization methods*, SIAM Rev., 43 (2001), pp. 89–112.
[30] C. Helzel, J. A. Rossmanith, and B. Taetz, *An unstaggered constrained transport method for the 3D ideal magnetohydrodynamic equations*, J. Comput. Phys., 230 (2011), pp. 3803–3829.
[31] C. Helzel, J. A. Rossmanith, and B. Taetz, *A high-order unstaggered constrained-transport method for the three-dimensional ideal magnetohydrodynamic equations based on the method of lines*, SIAM J. Sci. Comput., 35 (2013), pp. A623–A651.
[32] G.-S. Jiang and D. Peng, *Weighted ENO schemes for Hamilton–Jacobi equations*, SIAM J. Sci. Comput., 21 (2000), pp. 2126–2143.
[33] G.-S. Jiang and C.-W. Shu, *Efficient implementation of weighted ENO schemes*, J. Comput. Phys., 126 (1996), pp. 202–228.
[34] S. Kawai, *Divergence-free-preserving high-order schemes for magnetohydrodynamics: An artificial magnetic resistivity method*, J. Comput. Phys., 251 (2013), pp. 292–318.
[35] R. J. LeVeque, *Wave propagation algorithms for multidimensional hyperbolic systems*, J. Comput. Phys., 131 (1997), pp. 327–353.
[36] F. Li, L. Xu, and S. Yakovlev, *Central discontinuous Galerkin methods for ideal MHD equations with the exactly divergence-free magnetic field*, J. Comput. Phys., 230 (2011), pp. 4828–4847.
[37] P. Londrillo and L. Del Zanna, *High-order upwind schemes for multidimensional magnetohydrodynamics*, Astrophys. J., 530 (2000), p. 508.
[38] P. Londrillo and L. Del Zanna, *On the divergence-free condition in Godunov-type schemes for ideal magnetohydrodynamics: The upwind constrained transport method*, J. Comput. Phys., 195 (2004), pp. 17–48.
[39] G. K. Parks, *Physics of Space Plasmas—An Introduction*, Addison-Wesley, Reoding, MA 1991.
[40] K. G. Powell, *An Approximate Riemann Solver for Magnetohydrodynamics (That Works in More Than One Dimension)*, tech. report, Institute for Computer Applications in Science and Engineering, Hampton VA, 1994.
[41] K. G. Powell, P. L. Roe, T. J. Linde, T. I. Gombosi, and D. L. De Zeeuw, *A solution-adaptive upwind scheme for ideal magnetohydrodynamics*, J. Comput. Phys., 154 (1999), pp. 284–309.
[42] J. A. Rossmanith, *An unstaggered, high-resolution constrained transport method for magnetohydrodynamic flows*, SIAM J. Sci. Comput., 28 (2006), pp. 1766–1797.
[43] D. Ryu, F. Miniati, T. Jones, and A. Frank, *A divergence-free upwind code for multidimensional magnetohydrodynamic flows*, Astrophys. J., 509 (1998), p. 244.
[44] D. C. Seal, Q. Tang, Z. Xu, and A. J. Christlieb, *An explicit high-order single-stage single-step positivity-preserving finite difference WENO method for the compressible Euler equations*, J. Sci. Comput., 68 (2016), pp. 171–190.
[45] M. Torrilhon, *Locally divergence-preserving upwind finite volume schemes for magnetohydrodynamic equations*, SIAM J. Sci. Comput., 26 (2005), pp. 1166–1191.
[46] G. Tóth, *The $\nabla \cdot B = 0$ constraint in shock-capturing magnetohydrodynamics codes*, J. Comput. Phys., 161 (2000), pp. 605–652.
[47] J. R. Wilson, *Some magnetic effects in stellar collapse and accretion*, Ann. New York Acad. Sci., 262 (1975), pp. 123–132.
[48] K. Yee, *Numerical solution of initial boundary value problems involving Maxwell's equations in isotropic media*, IEEE Trans. Antennas and Propagation, 14 (1966), pp. 302–307.